RESEARCH PAPER

Localized deformation in intensely fissured clays studied by 2D digital image correlation

C. Vitone · G. Viggiani · F. Cotecchia ·
S. A. Hall

Abstract This paper represents a further step in a long-standing research on the influence of fissuring on the mechanical behavior of natural clays. The results of an experimental investigation into the influence of fissure orientation on the evolution of strain localization in the intensely fissured scaly clay from Santa Croce di Magliano (south of Italy) are reported. The experimental program involved plane strain compression tests where the effects of the combination of different factors, such as the specimen size and the orientation of fissuring, were investigated. A key aspect to this work is that the standard global stress–strain measurements were augmented by full-field displacement and strain measurements through 2D digital image correlation. Access to incremental strain fields provided information about slight details or anomalies as well as the complexity of deformation processes, which is of crucial importance for proper interpretation of test results at the global, macroscopic level.

Keywords Digital image correlation · Fissured clays · Fissuring orientation · Mechanical behavior · REV · Strain localization

C. Vitone (✉) · F. Cotecchia
Technical University of Bari, Bari, Italy
e-mail: c.vitone@poliba.it

G. Viggiani · S. A. Hall
UJF-Grenoble 1, Grenoble-INP, CNRS UMR 5521, Laboratoire
3SR, 38041 Grenoble, France

Present Address:
S. A. Hall
Division of Solid Mechanics, Lund University, Lund, Sweden

1 Introduction

Soils within geologic chain areas have generally experienced rather complex loading histories as a result of the tectonic processes. Consequently, they often possess a 'disturbed' structure, which makes them behave rather differently from other natural soils. Such disturbed soils usually referred to as *structurally complex formations* (e.g., [1, 11]) are generally characterized by structural features such as fissuring and abrupt variation in consistency. Fissuring, in particular, makes a clay significantly weaker than an unfissured one [33] and may be responsible for severe engineering problems (e.g., [2, 10, 26]).

The object of this study is a very highly fissured clay that outcrops in Santa Croce di Magliano, a small town in the southern Italian Apennines—referred to as *SCM scaly clay*, hereafter. During its geological history, this clay was subjected to large deformations due to tectonic processes, resulting in an intense network of fissures that split the clay into millimeter-sized lens-shaped elements (known as *scales*—which is the origin of their being referred to as *scaly clays* in the literature).

This paper represents a further step in a longstanding research program at the Technical University of Bari into the influence of fissuring on the mechanical behavior of natural clays. The research has been developed by means of the experimental study of several different fissured clays, including SCM scaly clay (see [38] for an overview). In a previous laboratory study on SCM scaly clay [40], it was shown by means of false relief stereophotogrammetry that, when the orientation of the fissures in the specimen is either random or normal to the direction of the maximum principal stress, the development of localized deformation during plane strain testing is not dictated by the preexisting fissures. Therefore, when this is the case, the shear band

develops in a similar way to what observed for unfissured clays. The present paper reports further data and interpretations about the influence of fissuring orientation on the evolution of strain localization in scaly clays, as resulting from recent new investigations. In particular, the objective is to define for which fissure orientations the localization process becomes strongly affected by the preexisting fissure network from the very beginning of the test. Here forth, the effect of the fissuring orientation in clay mechanics is investigated, based upon the analysis of both the global stress–strain response during plane strain compression tests and the evolution of displacements and strain fields throughout the specimen in the same tests. The analysis of the strain fields has been carried out by means of 2D digital image correlation (DIC).

The paper first presents the origin and physical properties of SCM scaly clay along with a characterization of its mesostructure. The experimental setup and the DIC method are then described before a detailed discussion of a few selected results. In particular, the discussion focuses on the influence of the fissuring orientation on the clay peak strength, global stress–strain behavior, and mechanisms of strain localization for different specimen sizes.

2 Material tested

The intensely fissured clays under investigation outcrop in Santa Croce di Magliano, a small town in the Daunia region located within the northeastern margin of the southern Italian Apennines. The Apenninic thrust system is part of the Mediterranean orogenic system that developed from the Late Cretaceous to Quaternary during the west-dipping subduction of the Adriatic-African plate under the European plate [14, 21].

The southern Apennines result from the tectonic juxtaposition of several tectono-stratigraphic units, and the clays in this study belong to the Daunia unit (see Fig. 1). Note that the extremely complex and intense fissuring network in these clays can be explained by considering that they belong to the most ancient formation, that is, an Oligocene–Miocene succession of clayey and calcareous strata (referred to as Red Flysch Formation by Dazzaro and Rapisardi [12], and Undifferentiated Clayey Complex by Melidoro et al. [23]). It has been observed that, in particular when fissuring is due to tectonic processes, the intensity of the fissuring pattern is directly proportional to both the complexity and age of the geological history experienced by the soils [38].

Both the extremely high shear strain and the large displacements experienced by the SCM clays during the Apennine orogenesis are responsible for the intense fissuring of the clay mesostructure. In particular, the fissure network
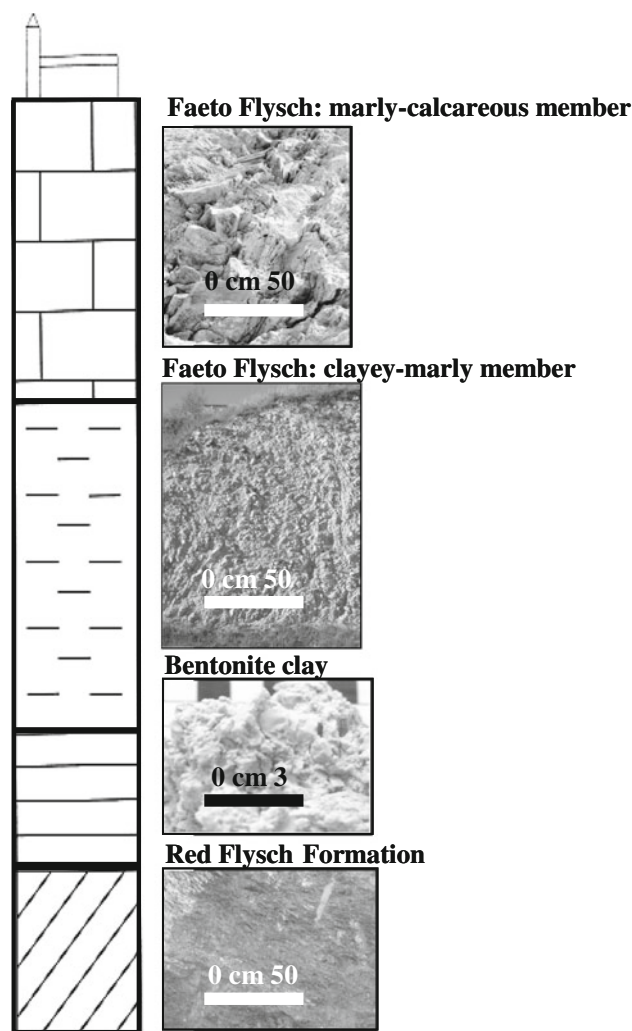

Fig. 1 Geological profile of the Daunia Unit at Santa Croce di Magliano

defines a *scaly mesofabric*, consisting of lens-shaped fragments of firm clay (the *scales*) of centimeter to millimeter size in length and millimeter size in thickness. Each *scale* can be in turn characterized by a 'scale-in-scale' fabric, of millimeter size in both length and thickness, which is referred to as *minifabric* (see Fig. 2). The *scales* are not bonded to each other (i.e., there is no inter-*scale* bonding), although some strong diagenetic bonding, due to tectonic loading, may exist inside the *scales* (intra-*scale* bonding).

The mesostructural features of SCM scaly clay have been analyzed and classified by means of the characterization chart proposed by Vitone et al. [39]. Figure 3 shows the 'Fissuring IDentity chart' (F-ID chart, hereafter) of the SCM scaly clay, in which the features that better characterize the mesostructure of SCM scaly clay are highlighted. In particular, the F-ID chart shows that the *scales* are firm to soft (B3 to B4 in the chart), whereas the discontinuities
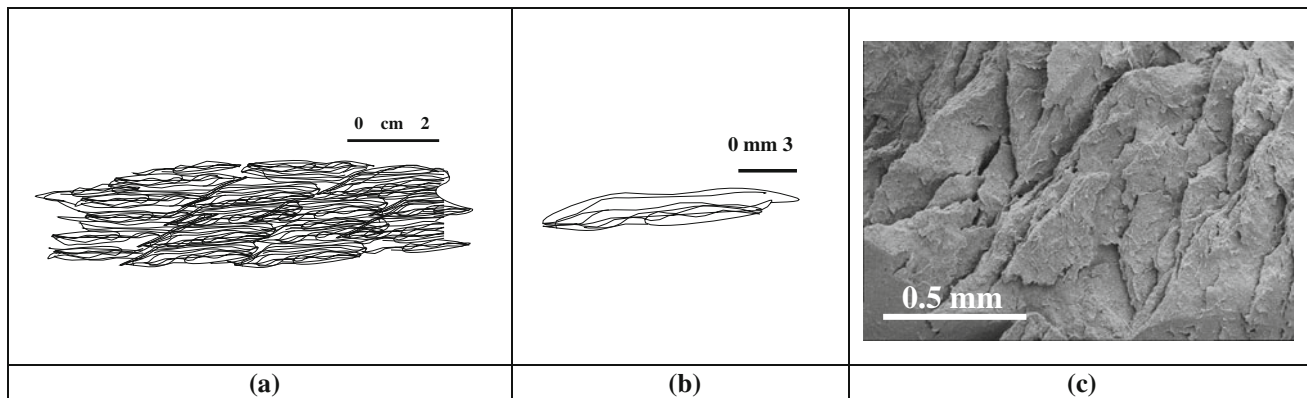
Fig. 2 a Sketch of the scaly mesofabric; **b** *scale-in-scale* fabric within a *scale*; **c** SEM picture at low enlargement of the scaly minifabric in its natural state

are smooth to slickensided (D4 to D6), fresh to weathered (E1 to E3), and the fissure surfaces appear planar (G1). At the scale of a laboratory specimen, there is one single prevailing direction of the *scales*, so that also fissuring orientation is about single (F1-$X°$, where $X°$ is the value, in degrees, of the fissure orientation with respect to the horizontal). The intensity of the fissuring surrounding the *scales* is the highest possible (I6) in the F-ID chart, due to both the small average volume of the *scales* and their very high specific surface (about 0.3 cm^3 and 1,000 m^2/m^3, respectively). Furthermore, given the continuity of several mildly undulated fissures that envelope the strata formed of *scales*, the fissuring network of SCM scaly clay is characterized by many intersections (H2), according to the F-ID chart in Fig. 3.

The SCM clay includes small quantities of kaolinite and chlorite and a large amount of illite–smectite mixed-layer clay minerals (about 80 %), with 50 % of smectite (as measured through X-ray diffraction, [8]). The clay fraction is equal to 91 % and the plasticity index is about 52 %, such that the clay is of medium activity ($A = 0.57$), according to standard geotechnical testing. The SCM clay can be classified as CH in the Unified Soil Classification System.

The specimens of SCM clay used in the mechanical testing were extracted within a Red Flysch outcropping at about 3 m below ground level (Fig. 4), after removal of a thick soil layer. The samples were taken about 3 meters above the water table. Figure 4 also shows the unconventional sampling technique being adopted, which involved on-purpose designed C-shaped steel samplers (Fig. 4a) that were inserted into the soil (Fig. 4c, d) after lubricating their inner surface with silicon oil. The samplers were extracted after removal of the surrounding soil (Fig. 4e, f). Thereafter, each full sampler was wrapped in cling film and waxed in situ, in order to minimize the loss of water content of the clay, and finally stored in a moisture control chamber. For further details about the sampling technique, see also [41].

3 Experimental setup and digital image correlation

The mechanical tests of this study were performed in the plane strain apparatus at Laboratoire 3SR in Grenoble (Fig. 5a, b; see [13], for further details). In each test, 35-mm-thick prismatic specimens were mounted between two rigid walls, which induce plane strain conditions. These rigid walls are transparent glass plates, which permit digital photographs to be taken of the in-plane surface of the specimen during a test (Fig. 5b). The top loading platen is free to slide horizontally in the plane of deformation, which allows free lateral displacement of the upper portion of the specimen, for example, when a shear band forms due to deviatoric loading. All surfaces in contact with the specimen are lubricated with silicone grease to minimize friction. High-resolution photographs of the scaly clay specimen were taken throughout the tests for subsequent DIC analysis. In this study, a 13.8 MPixel digital camera (Kodak DCS Pro 14 N) was used. The pixel size of the acquired images was between 27 and 40 μm, depending on the size of the specimens. The photographed surface of the specimens was illuminated using cold lamps (Starlight lamps—nominal power tubes: 110 W; tubes frequency: 40,000 Hz; color temperature: 5,400°K—see Fig. 5b), in order to avoid overheating that would accelerate the reduction in saturation of the soil.

DIC is a non-contact method used to provide full-field measurements of displacement fields at the surface of objects under any kind of loading based on the numerical comparison between two digital images. The application of DIC has become increasingly common over the past 20–30 years in many branches of mechanics and has also seen increasing usage for the monitoring of deformation in soil mechanics laboratory experiments (e.g., [18, 28, 43]); see Viggiani and Hall [36] for a review of the information that DIC can provide about the features of strain localization in geomaterials. To the best of our knowledge, the

	INTACT SOIL		DISCONTINUITY NATURE			DISCONTINUITY ORIENTATION[1]	DISCONTINUITY GEOMETRY		
	Main sediment fraction **A**	*Undrained strength* [2] **B**	*Type* **C**	*Roughness* [3] **D**	*State* **E**	**F**	*Shape* [4] **G**	*Continuity* [4] **H**	*Intensity* [5] **I**
1	**Clay**	Mudstone	Depositional	Very rough	**Fresh**	**Single**	**Planar**	Continuous	Rare: $<3m^2/m^3 ->1m^3$
2	Silt	Stiff clay	Stress relief	Rough	**Slightly weathered**	Few	Curved	**Many intersections**	Very low: $3\div10$ m²/m³ - $0.027\div1$ m³
3	Silty clay	**Firm clay**	**Shear induced**	Slightly rough	**Highly weathered**	Random	Hinged	Some intersections	Low: $10\div30$ m²/m³- $0.001\div0.027$ m³
4	Clayey silt	**Soft clay**		**Smooth**	Iron stained surfaces		Folded	Very few intersections	Medium: $30\div100$ m²/m³- $27\div1000$ cm³
5	Marly clay			**Very smooth**	Coated		Conchoidal		High: $100\div300$ m²/m³- $1\div27$ cm³
6				**Slickensided**					**Very high: >300m²/m³ - <1cm³**

Fig. 3 F-ID chart of the SCM scaly clay. *1* With respect to the horizontal direction, *2* after Morgenstern and Eigenbrod [24] and BS 8004 [6], *3* sandpaper grade [16]; roughness classification [20], *4* after Coffey & Partners in Walker et al. [42], *5* area of discontinuities per unit volume (m²/m³) and/or average size (m³, cm³) of the intact peds/blocks (after [16], modified)
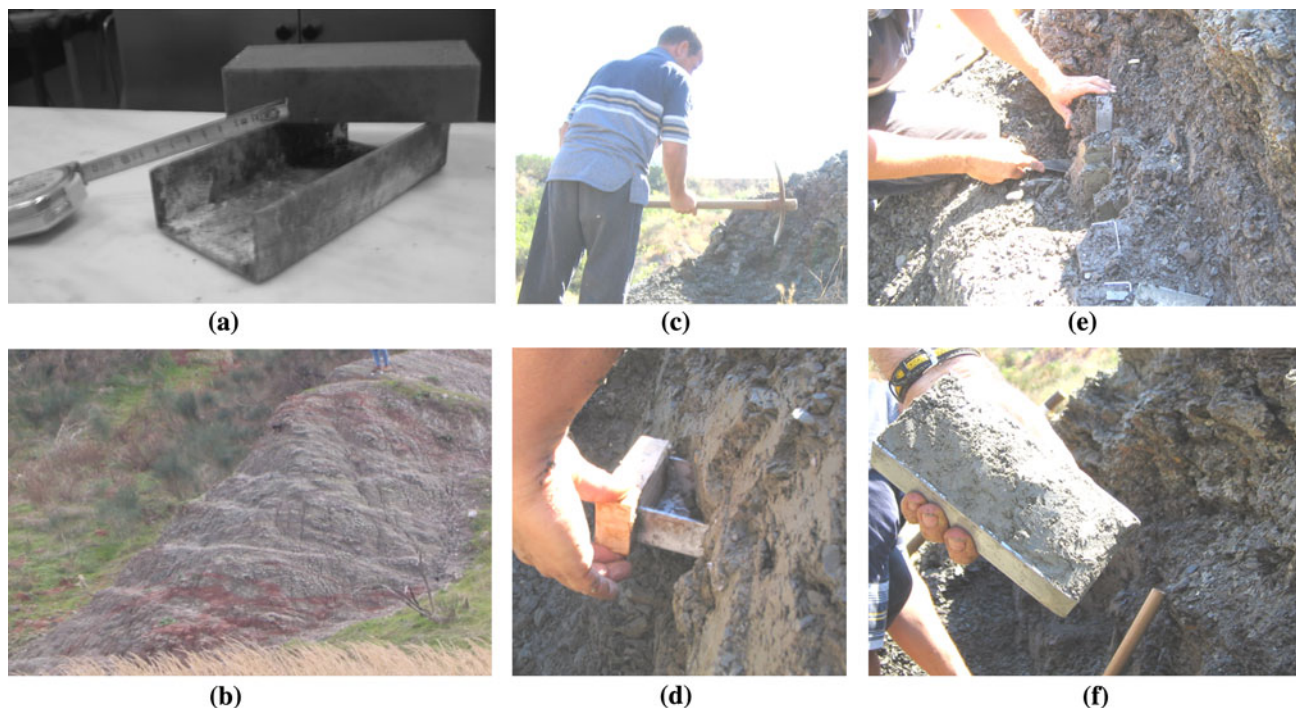

Fig. 4 Sampling SCM scaly clays: **a** sampler and extractor; **b** sampling site; **c** removal of a thick stratum of soil; **d**, **e** insertion of the C-shaped steel samplers; **f** full sampler extracted from the soil
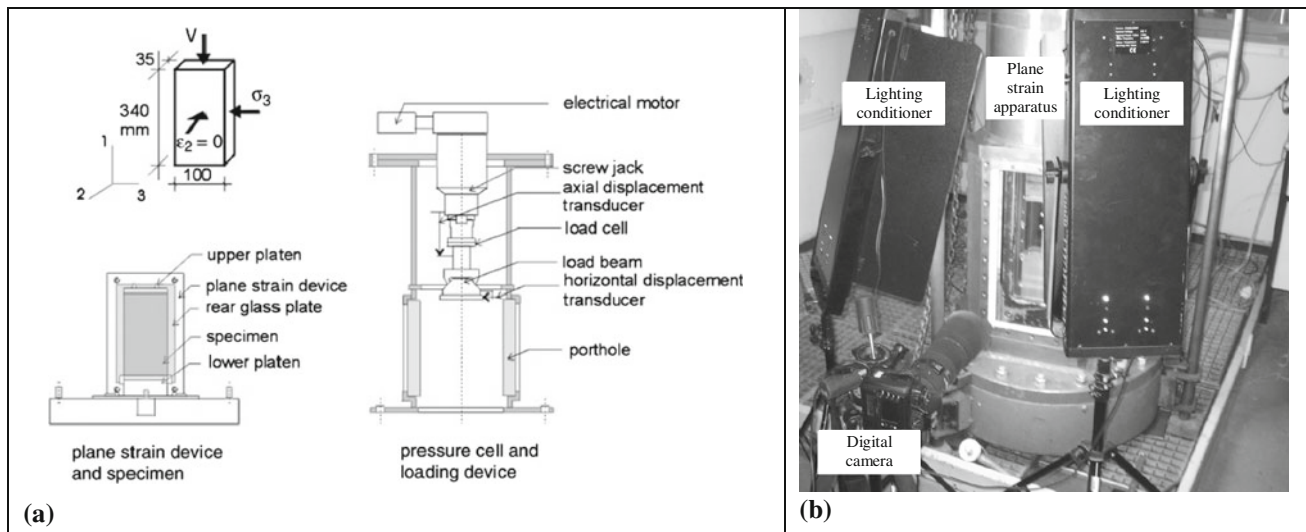
Fig. 5 **a** Sketch of the plane strain apparatus and the maximum size of the specimen that can be tested (from [13]); **b** plane strain test setup: apparatus, high-resolution digital camera, cold lamps

present study is the first in which the method has been applied to natural fissured clays.

DIC can be considered as a process of mapping one digital image into another. In the current application, digital images of the clay specimens, taken at different stages of deformation during a test, are divided into many small regions that are then associated from one image to the next; the image transformation of each of these small regions that provides the best match between the images yields the surface displacement field. In this context, the first image is referred to as the 'reference image' and the second one the 'deformed image'. The DIC procedure starts by dividing the reference image into square domains (the 'correlation windows' or 'subsets') and, for each of these subsets, a search is performed in the second image for the most similar subset, in terms of the image gray levels. The transformation of the reference image into the deformed image is described by the displacement and the deformation of the subset that gives the best image match (so that the squares might become quadrilaterals in the second image). A correlation coefficient quantifies the similarity of the subsets in the two configurations. In this study, DIC was performed using the software 7D, developed at the University of Annecy, France; for the full technical details, such as the sub-pixel refinement procedure, see [34]. In this study, the image subsets used were squares of side 10 pixels and the spacing between their centers was also 10 pixels.

To increase the accuracy and precision of the DIC, the image textures were augmented by applying a 'speckle pattern' to the surfaces of the specimens (the SCM clay specimen surfaces were already naturally textured, but an improved DIC result could be achieved with the additional speckle). Speckle patterns are spots that, in this case, are sprayed using an aerosol spray paint over the surface of the specimen. This speckle textured surface provided higher image contrast for the specimens at the scale of the measurement that could be easily identified in the acquired photographs. This technique ensured the possibility of identifying uniquely each image subset from one image to the next (see [22], for more technical details).

While the DIC procedure used herein is based upon finding the optimal displacements and deformations to map the subsets, the strains that will be presented in Sect. 5 are computed from the local differences of the nodal displacements. These strain tensors are most efficiently visualized in terms of volumetric and maximum shear strains, which are, respectively, defined as

$$\varepsilon_v = \varepsilon_1 + \varepsilon_3,$$

$$\varepsilon_s = 1/2(\varepsilon_1 - \varepsilon_3),$$

where ε_1 and ε_3 are the major and minor (logarithmic) strains, respectively.

It is important to realize that the DIC approach used herein is essentially a piecewise continuum analysis, that is, continuity is assumed within each subset. Furthermore, the calculation of strains from the nodal displacements assumes continuity between subsets. It is therefore inherently assumed that no strong discontinuities (i.e., discontinuities of displacement) exist between the images. However, for SCM scaly clay, the deformation processes often consisted of relative displacements along preexisting fissures. In other words, strong discontinuities do exist in these tests, and the continuum condition can be locally violated. Therefore, while DIC provides a correct analysis of the displacement and strain of blocks around the

developing fissures, deformation cannot always be properly described in terms of strain in the region of the fissures. The implication of this is that strain values computed across fissures should be considered as smeared representations of displacement discontinuities; shear strain being an indicator of sliding and volumetric strain indicating opening/closing of fissures. If, on the contrary, the objective is a quantitative analysis of discontinuous deformation, then non-standard DIC methods must be used, with adequate data acquisition and processing strategies to allow the displacement jump across the discontinuity to be computed and represented—rather than smearing it in a necessarily non-objective local strain concentration.

A number of recent publications have employed DIC to experimentally study discontinuous deformation, including 'standard' DIC for dynamic crack tip location [17] and stress intensity factor measurement [29, 32, 44], 'extended' DIC (X-DIC; [7, 30, 31]), and a 'subset-splitting' method [27]. Interestingly, Nguyen et al. [25] suggested an extended DIC method, based on post-processing of DIC results with the same 7D software used in the present study. This approach has been tested for the images in the present study, but is not discussed further as it does not add significant new insight into the deformation processes here of interest.

4 Testing program

Plane strain compression tests were performed at zero confining pressure (i.e., the minor principal total stress σ_3 was zero throughout each test), without any re-saturation or consolidation of the specimen prior to loading. Loading was performed under displacement control, with a rate of applied axial (vertical) displacement of 0.006 mm/min. The top platen was free both to rotate and to translate in the plane of deformation in all tests.

The initial values of void ratio and degree of saturation were 0.820–0.990 and 72–86 %, respectively. While the clay *scales* were fully saturated, the specimen saturation was below 100 % mainly due to the presence of open fissures. See also [38] for further details about the initial state of SCM scaly clay. In addition, fissure opening and air entry could take place in the specimens during the tests since they were not either confined or under controlled saturation. Therefore, it can be envisaged that the strain fields at late stage of testing would be probably different from those observed under the conditions here outlined if the specimens had been confined and saturated. Table 1 summarizes the experimental program conducted in this study, which consisted of a total of 10 tests.

The mesostructural features of the clay specimens made the test setup generally quite difficult, starting from sample extraction, which was everything but an obvious operation. During extraction, the specimens were carefully trimmed down to the size required for testing, since the size of the samplers was slightly larger than the specimen size. The surfaces were smoothed and made perpendicular to each other. Finally, the specimen was mounted between the two rigid thick glass walls of the plane strain device, without any membrane (see Fig. 5b). Note that, due to the difficulties in specimen preparation, the dimensions of similar-size specimens were not exactly the same. In particular, their initial nominal height and width (in the plane of deformation) were set to be about 40–80 mm for the small specimens and about 75–150 mm for the large ones (Table 1).

In the following, a letter/number naming scheme has been used to present the tests, where the first letter refers to the specimen size (S for small, L for large), the 2nd letter to the fissure orientation (H for horizontal, Sub for sub-horizontal, M for medium, V for vertical), and a sequential number is used when more than one test has been performed under the same conditions.

Seven tests were performed on specimens having either horizontal or sub-horizontal fissures (i.e., inclination up to 30° to the horizontal; large specimens: L-Sub, LH1, LH2; small specimens: S-Sub, SH1, SH2, SH3). In the other three tests (small specimens: SM and SV; large specimen: LM), the fissures had higher inclination (from 50° to 90°) to the horizontal (Table 1).

Specimens SH3 and LH1 were equipped with acoustic emission (AE, hereafter) transducers (Physical Acoustic Corporation, PAC, transducers, type R15).
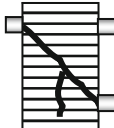
In the following, only few selected results will be discussed. In particular, Vitone et al. [40] already presented the patterns of localized deformation followed by the small specimens SH1 and SH2 with horizontal fissures during plane strain tests. Vitone et al. [40] analyzed the clay specimen deformation using false relief stereophotogrammetry (FRS hereafter). The results of the stereophotogrammetric analysis appeared to confirm those of specimen L-Sub carried out making use of DIC and here presented.

5 Results

5.1 Global responses

Figure 6 shows the stress–strain curves resulting from seven tests in which the SCM scaly clay specimens had different sizes and fissure orientations; horizontal to sub-horizontal (Fig. 6a), medium (Fig. 6b), and vertical (Fig. 6c) inclinations were considered. In all the tests, localized deformation was observed to take place in the specimen. In the presence of such localized deformation, it is clear that the meaning of stress and strain derived from

Table 1 Summary of the plane strain compression tests performed in the present study

Test		Specimen dimensions	Fissure inclination to the horizontal (degrees)	Sketch of the specimen at the end of the test
1	SH1	Small	Horizontal fissures (0°)	
2	SH2	Small	Horizontal fissures (0°)	
3	SH3[a]	Small	Horizontal fissures (0°)	
4	LH1[a]	Large	Horizontal fissures (0°)	
5	LH2	Large	Horizontal fissures (0°)	
6	L-Sub	Large	Horizontal and sub-horizontal fissures (0°–20°)	
7	S-Sub	Small	Sub-horizontal fissures (30°)	
8	SM	Small	Fissures with medium inclination (50°)	
9	LM	Large	Fissures with medium inclination (50°)	
10	SV	Small	Vertical fissures (90°)	

[a] Specimen equipped with acoustic emission transducers

boundary measurements of loads and displacements is only nominal, or conventional. Therefore, the curves of Fig. 6 should be seen as an overall response of the specimen and not as the constitutive response of the material.

Specimens SH2 and L-Sub (Fig. 6a) having horizontal and sub-horizontal fissure orientation exhibit similar stress–strain response and peak strength irrespective of the differences in dimensions (Table 1). This is consistent with previous observations from triaxial compression tests on SCM scaly clays reported by Vitone et al. [40] and Vitone and Cotecchia [38], according to which the authors

suggested that a standard (38 mm diameter) triaxial specimen is large enough to be considered as a representative element volume (REV) for very highly fissured clays (I6 clay in Fig. 3) of either random fissures (F3) or oriented horizontal fissures (i.e., F1-0°). In particular, this was the case if the REV represents the minimum specimen size including a number of fissures large enough to represent the general recurrence of fissures in the material and therefore to exhibit the behavior of any larger specimen [9].

In Fig. 6a is also reported the stress–strain curve of the F1-0° large specimen LH1 as representative of the effect on
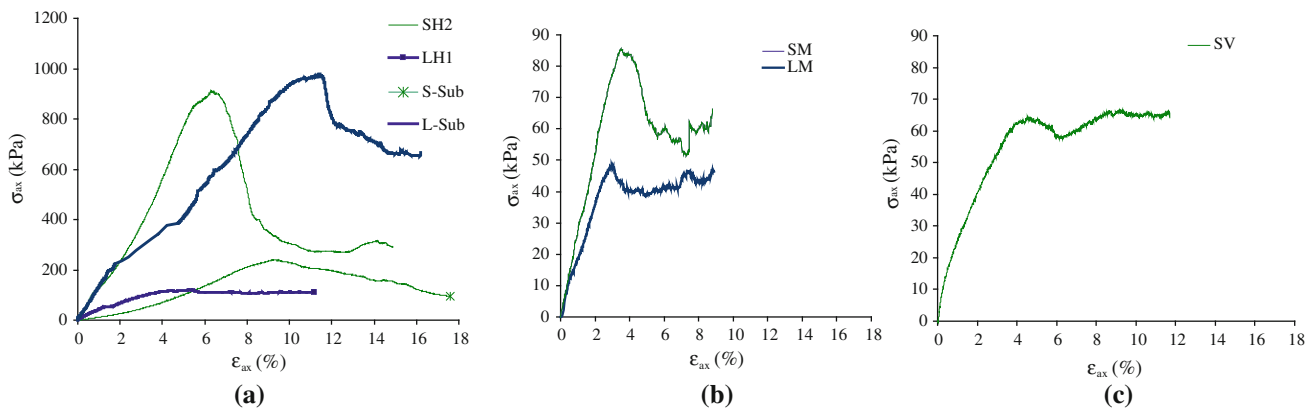
Fig. 6 Stress–strain curves: **a** horizontal and sub-horizontal fissures; **b** medium inclined fissures; **c** vertical fissures. *Bold curves* refer to large specimens, *thin curves* to small

the overall clay strength of the disturbance produced by the AE transducers placed on the opposite sides of the specimen. In particular, as discussed later in the paper, both the specimens equipped with AE transducers (i.e., SH3 and LH1) failed prematurely on medium inclined and continuous fissures that were *artificially* induced.

However, also specimen S-Sub with sub-horizontal fissures (F1-30°), although not equipped with AE transducers, exhibited a peak axial stress significantly lower than the other two undisturbed specimens, SH2 and L-Sub. This has been probably due to the coalescence of preexisting fissures inclined of 30° to the horizontal, determining the formation of a single inclined surface that crossed almost the entire specimen and took control of its global response, as revealed by DIC and discussed later in the paper.

Figure 6a and the other data in Fig. 6b, c indicate that the orientation of fissuring influences the shear behavior of the SCM scaly clay specimens, since both the specimen strength and strain softening reduce with increasing fissure inclination. Figure 6b also shows that for medium inclined fissures (i.e., about 50° to the horizontal), the recorded strength is substantially higher for the smaller specimen (SM) than for the larger one (LM). This would suggest that, in this case, the smaller specimen could be too small to be considered as the REV for the clay. Note that, in agreement with this framework of behavior, from the comparison of the shearing behavior of small specimens in Fig. 6, it emerges that specimen SM, with fissures inclined at about 50° to the horizontal, exhibited maximum axial stress lower than specimens SH2 and S-Sub and higher than that of specimen SV with vertical fissures (F1-90°), which showed the minimum strength without softening.

The reduction in strain softening as the fissure inclination increases with respect to the horizontal can be quantified by means of a modified brittleness index [5], $I_B = (\sigma_p - \sigma_{pp})/\sigma_p$ (where σ_p and σ_{pp} are the peak and post-peak axial stresses, respectively). Figure 7 clearly
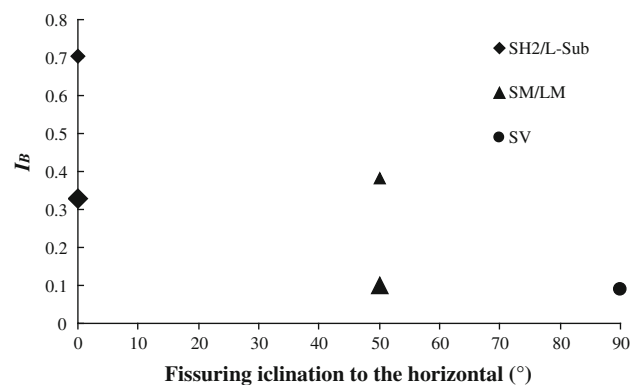

Fig. 7 I_B values recorded for the specimens of scaly clays. *Small* and *large symbols* refer to small and large specimens, respectively

shows that: (1) for a given inclination of the fissures, I_B reduces with increasing specimen size; (2) for a given specimen size, I_B reduces with increasing inclination of the fissures, which is also consistent with results obtained for other Italian scaly clays (e.g., [2–4, 15]).

5.2 DIC analysis of deformation processes

Results of DIC analyses carried out during six selected tests are shown in Figs. 8–13. The numbers of the photographs used in the analysis are noted on the force–displacement curves, which are shown for each test together with pictures of the specimen at the beginning and at the end of the test.

In particular, in the following, the discussion will make reference to the strain increments highlighted in red on the force–displacement curves in the figures. As a result of the analysis, the figures also show, for each investigated increment, maps of the magnitudes of the maximum shear strain, ε_s, in the upper row, and volumetric strain, ε_v, in the lower row. The size of the square symbols in these maps is proportional to the value of the relevant quantity (note that
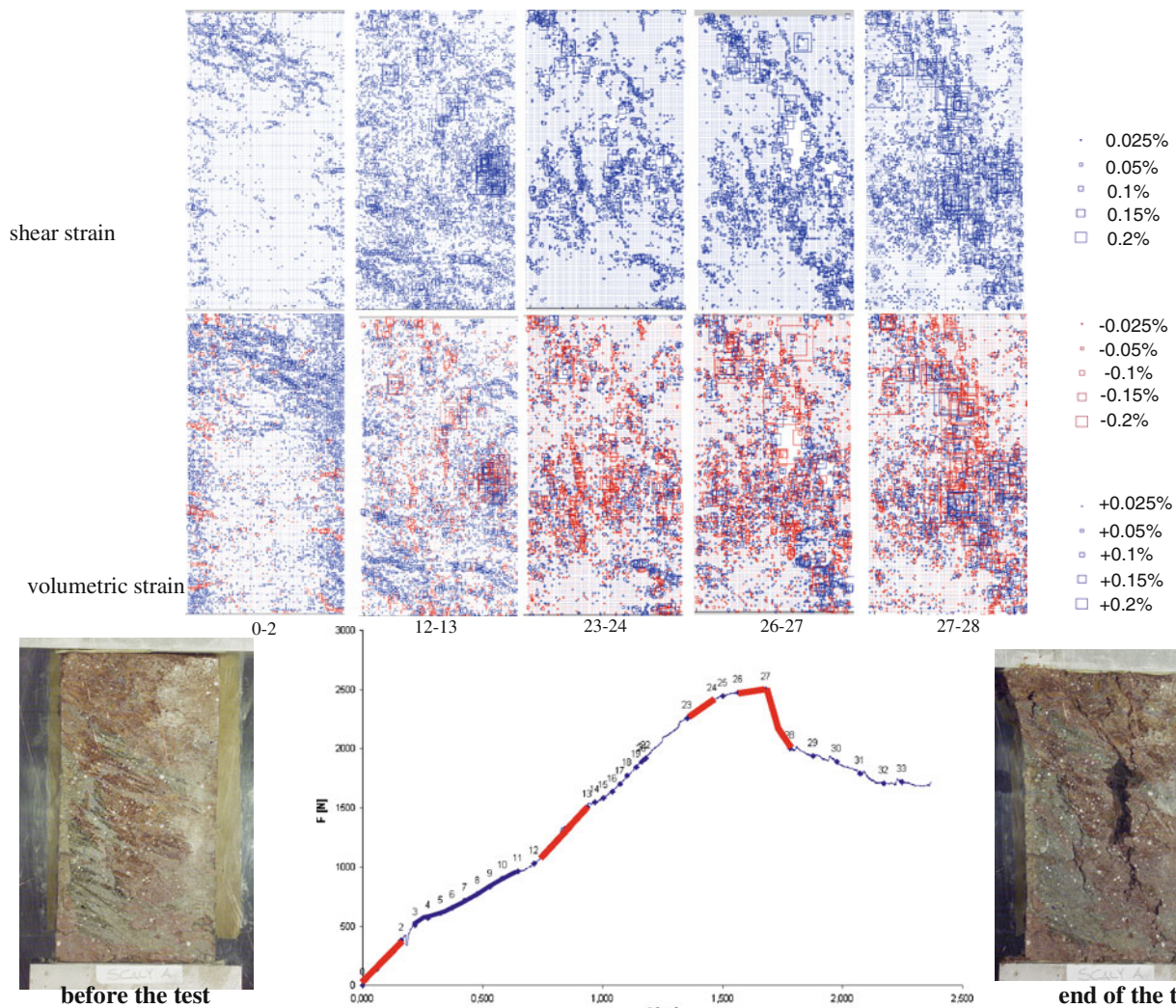
Fig. 8 Test L-Sub. Load–displacement curve and DIC-derived shear and volumetric strain fields for selected load increments (in *red* along the *curve*) (color figure online)

symbol scale is different for each investigated increment). For volumetric strain, red symbols refer to dilation and blue symbols to contraction.

5.3 Horizontal and sub-horizontal fissures (F1-0° to F1-30°)

Figure 8 shows the results of DIC for the test performed on the large specimen L-Sub, containing mainly horizontal fissures but also some sub-horizontal fissures (about F1-20) confined at the top of the specimen (see also the photograph of the specimen before the test). During increment 0–2, the upper portion of the specimen exhibited volumetric contraction, which corresponds to sealing of the continuous sub-horizontal fissures. The same regions experienced higher shear strains than the rest of the specimen, which indicates that compaction between the *scales*

was accompanied by their relative adjustment and sliding. At the same time, slight episodes of volume increase (i.e., fissure opening) occurred on the sides of the specimen. Later in the test, but still quite before peak (increment 12–13), localized regions of volume contraction were still visible over the entire height of the specimen, indicative of fissure closure across the whole specimen. In the same increment, 12–13, a few vertically aligned regions of dilative strain appeared within the specimen, corresponding to a new opening of fractures parallel to the specimen axis. These regions became more persistent and pronounced in the following increment 23–24, shortly before the stress peak, when they were also associated with localized shear straining.

The strain field was still relatively uniform in increment 26–27, at peak stress, although a pattern of localized deformation can be discerned, which becomes to some
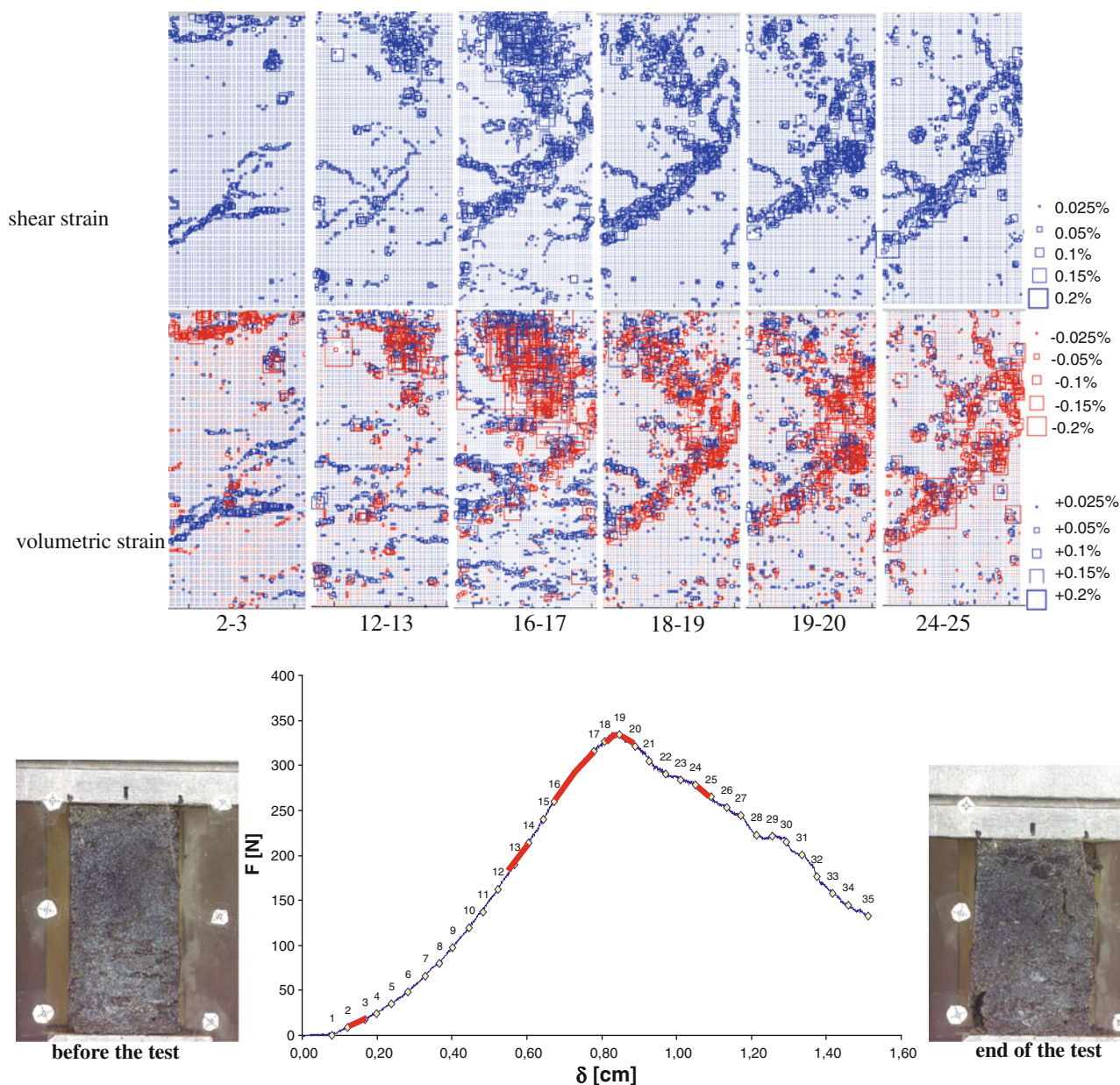
Fig. 9 Test S-Sub. Load–displacement curve and DIC-derived shear and volumetric strain fields for selected load increments (in *red* along the *curve*) (color figure online)

extent more pronounced in the post-peak increment 27–28. The photograph of the specimen at the end of the test clearly shows the complexity of the failure process including both opening and sliding discontinuities. In particular, it brought about the development of a shear band embodying the zones where shear strain mostly localized from stage 23 onwards (i.e., shortly before peak), and dilation was such as to cause local opening of fractures in the core of the specimen.

The localization process observed for specimen L-Sub is quite similar to that observed on either unfissured specimens (e.g., [35]) or small specimens with horizontal fissures, as shown for specimen SH2 by [40] by using FRS. Also, in these cases, non-uniform straining occurs shortly before the stress peak and develops fully post-peak. The similarity between the localization processes developing within the F1-0° large specimen L-Sub and the F1-0° small specimen SH2 is reflected by their similar global stress–strain response in Fig. 6a.

Figure 9 shows DIC-derived strain fields for some selected increments of the test on the small specimen S-Sub, with fissures inclined at 30° with respect to the horizontal. As in the case of the large specimen L-Sub, the early stages of the test were characterized by the closure of
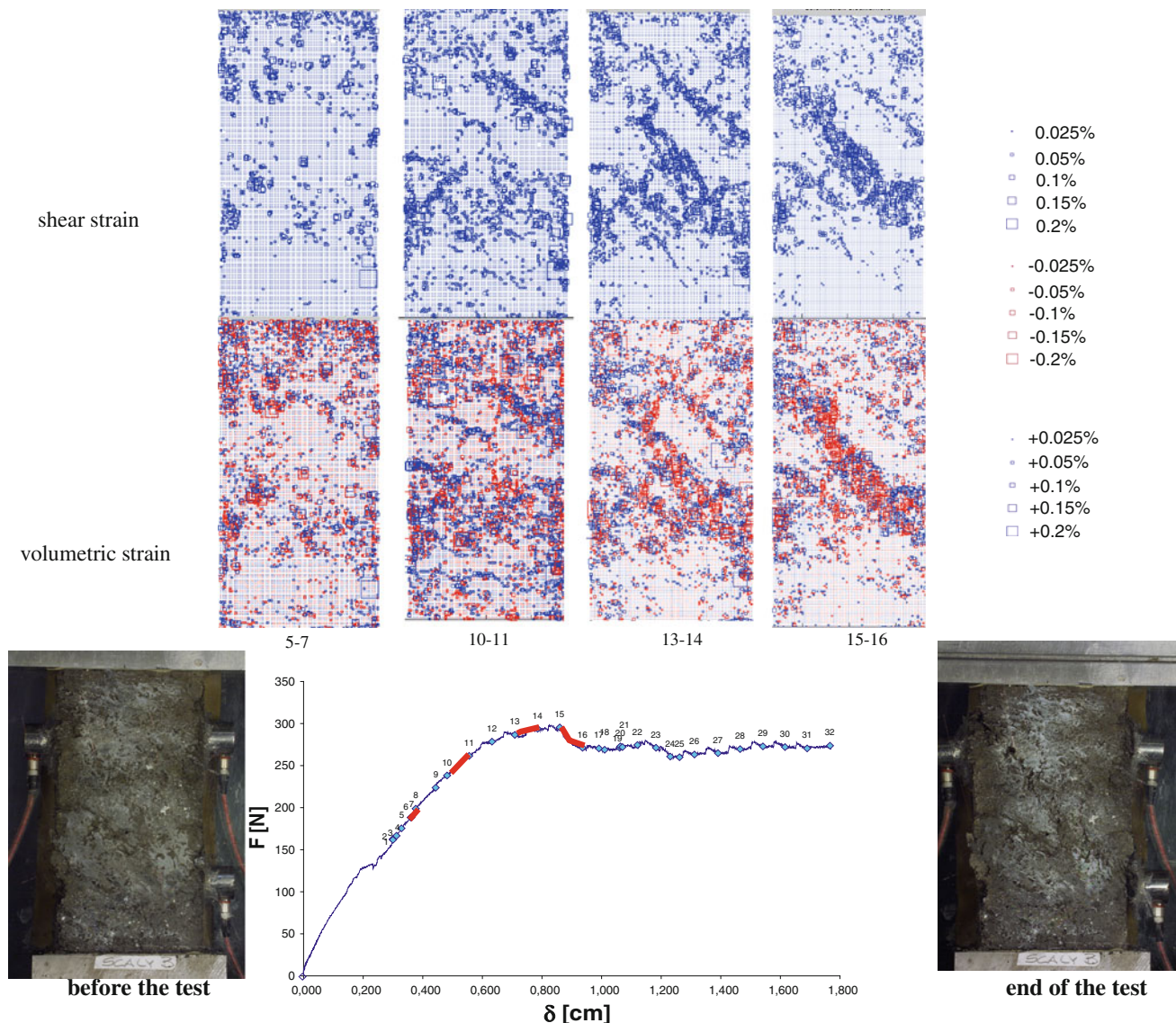
Fig. 10 Test LH1. Load–displacement curve and DIC-derived shear and volumetric strain fields for selected load increments (in *red* along the *curve*). The two photographs show before and at the end of the test the specimen and the three AE transducers (color figure online)

sub-horizontal fissures (see increments 2–3 and 12–13). However, differently from the previous case, at the very beginning of the test (increment 2–3), a well-defined region, crossing the entire specimen at an inclination of about 30°–40° to the horizontal, was visible, within which both contraction and sliding took place. It should be noted that there was no evidence of such a region on the surface of the specimen at the beginning of the test.

Starting from increment 16–17, before the peak, the strain fields are indicative of a sliding mechanism between two near-rigid bodies along the detected shear band. Interestingly, this final mechanism resembles very much the pattern of localized deformation that was observed at the beginning of the test. In this test, the activation of the sliding mechanism from earlier stages of testing makes the

maximum specimen strength lower than that of tests during which the peak strength was achieved before sliding onset (e.g., L-Sub; Fig. 6).

Figure 10 shows DIC-derived strain fields for some selected increments of the test on the large specimen LH1, with horizontal fissures. As for the other specimens, the early stages of the test were characterized by the closure of sub-horizontal fissures (see increments 5–7 and 10–11). However, as shown in Fig. 6, the specimen exhibited a maximum strength even lower than that of S-Sub. This was probably the effect of the sample disturbance caused by the three AE transducers mounted on the opposite sides of the specimen (see the photographs in Fig. 10). It has to be inferred that the weight of the transducers, which were glued to the specimen surface, has generated additional
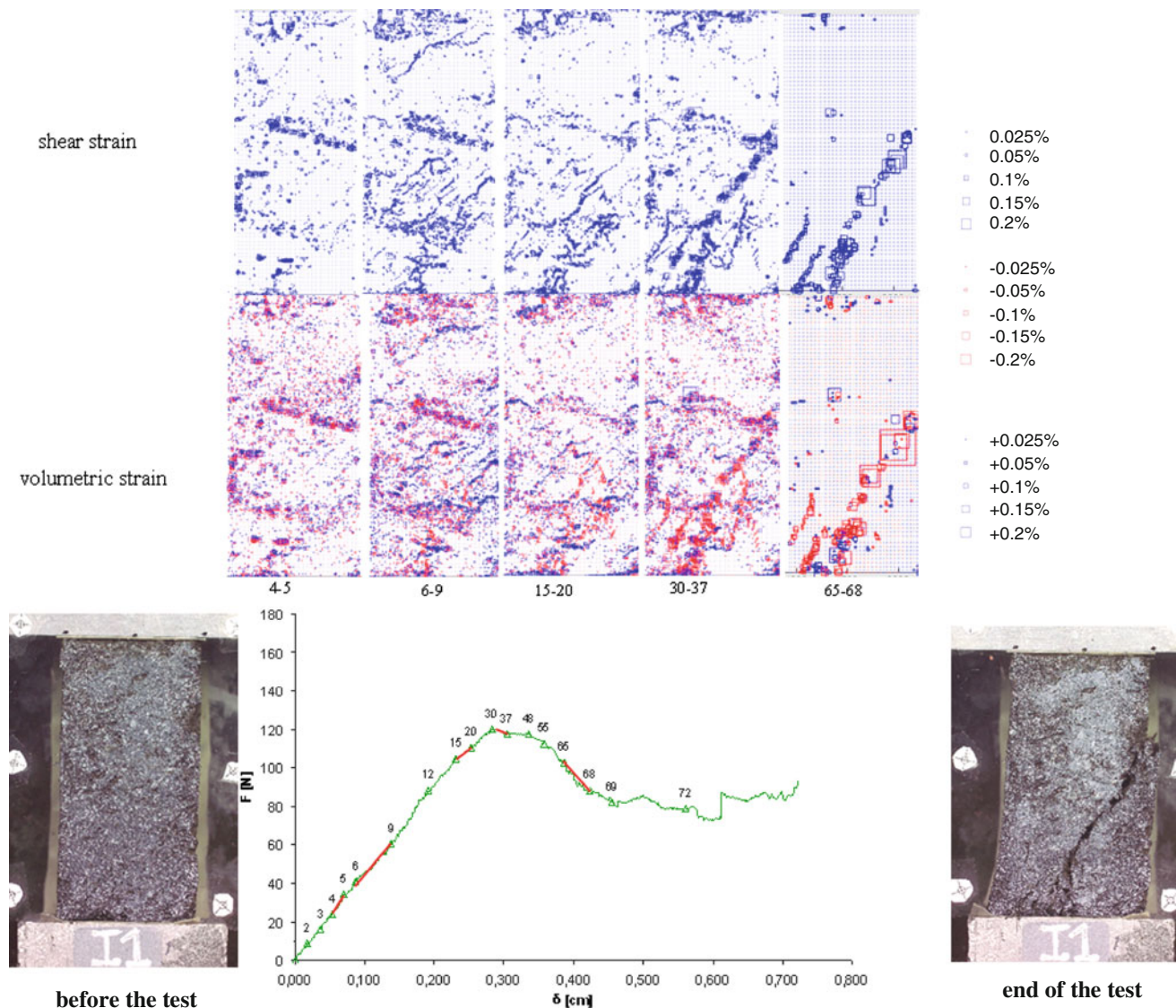
Fig. 11 Test SM. Load–displacement curve and DIC-derived shear and volumetric strain fields for selected load increments (in *red* along the *curve*) (color figure online)

loading that appears to have triggered the development of a premature shear band (increment 5–7), which was inclined at about 45° to the horizontal. In the following increments, the whole process consisted in the development of the localized area, which extended up to cross entirely the specimen. Therefore, from the early stages of the test, the process was that of sliding between near-rigid portions of the specimen. The effect of the 'induced' premature failure is that the global stress–strain behavior of the specimen is characterized by the lowest strength and the least brittle response. The same pattern of behavior was recorded during plane strain shearing when two AE transducers were mounted on the opposite sides of the small specimen SH3 (see [37] for further details). As for the specimen S-Sub, this specimen failed on two medium inclined (about 50° to the

horizontal) sliding surfaces which formed prematurely due to the presence of the AE transducers.

5.4 Medium inclination fissures (F1-50°)

Figures 11 and 12 illustrate the evolution of the strain fields during the two tests carried out on specimens having fissures inclined at about 50° to the horizontal (small specimen SM and large specimen LM, see Table 1).

In test SM (Fig. 11), multiple parallel zones of localized deformation formed in the lower portion of the specimen starting since increment 6–9, well before the peak. These correspond to the activation of preexisting fissures, inclined at 50° to the horizontal; both sliding and compaction took place at a number of such fissures, until one of them
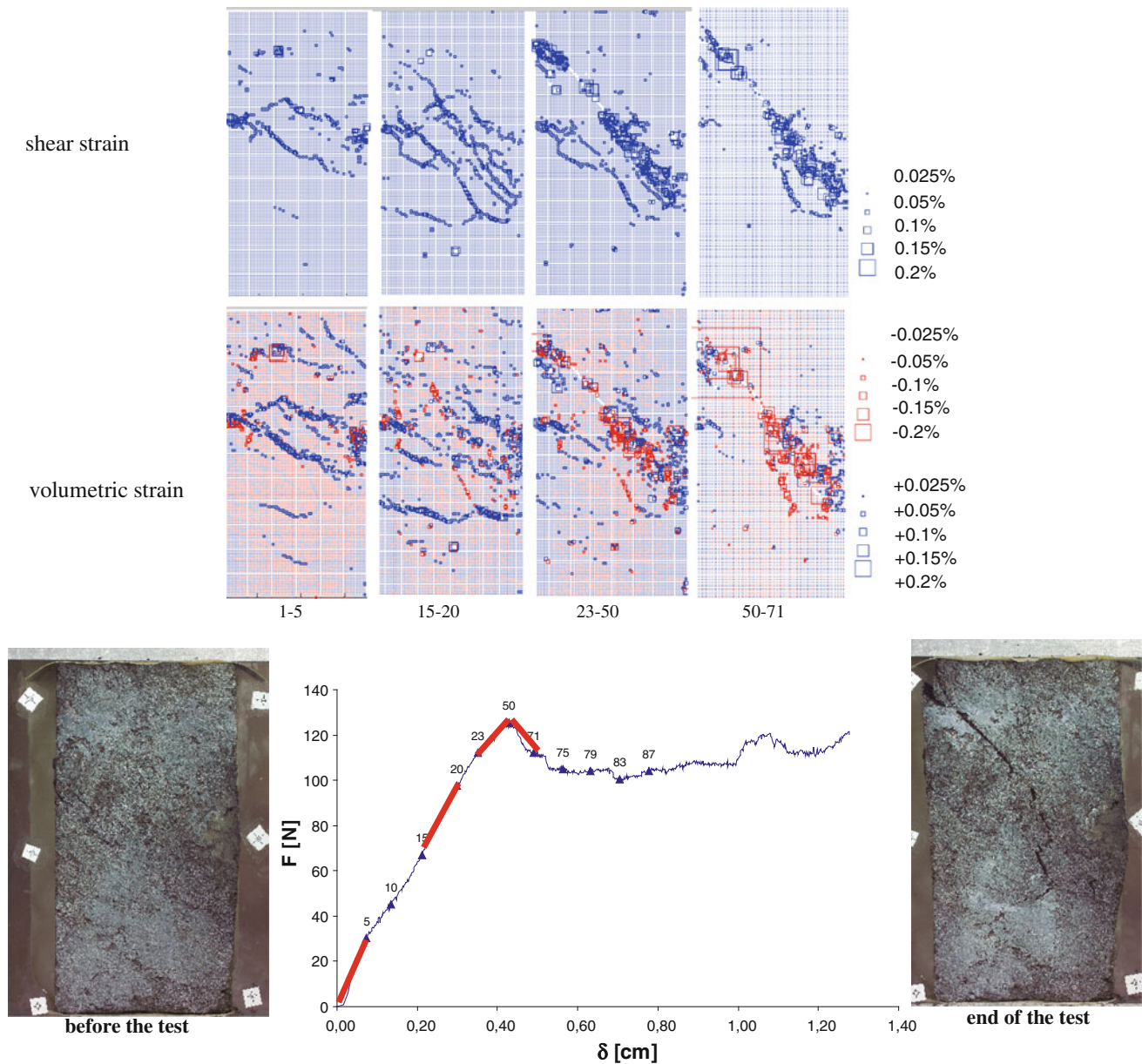
Fig. 12 Test LM. Load–displacement curve and DIC-derived shear and volumetric strain fields for selected load increments (in *red* along the curve) (color figure online)

eventually dominated—starting from increment 30–37 that is, around the peak—with fissure opening taking place during further sliding. The post-peak behavior consisted of two rigid bodies sliding over each other along a surface inclined at 50° to the horizontal (see increment 65–68). In all the increments except the post-peak one (65–68), a distinct sub-horizontal fissure was observed to close in the upper half of the specimen. Above this fissure, the specimen appears almost undeformed throughout the test.

The deformation process observed throughout the test on the large specimen LM (Fig. 12) is similar to that of test SM. It is dominated, since the very beginning of the test, by

a well-defined pattern of localized deformation inclined of 50° to the horizontal. As for specimen SM, relative sliding was associated with compaction (fissure closing) before the peak, and with dilation (fissure opening) afterwards. Again, the post-peak process consisted essentially of relative sliding of nearly rigid blocks. This was confirmed by the visual inspection of the specimen at the end of the test.

5.5 Vertical fissures (F1-90°)

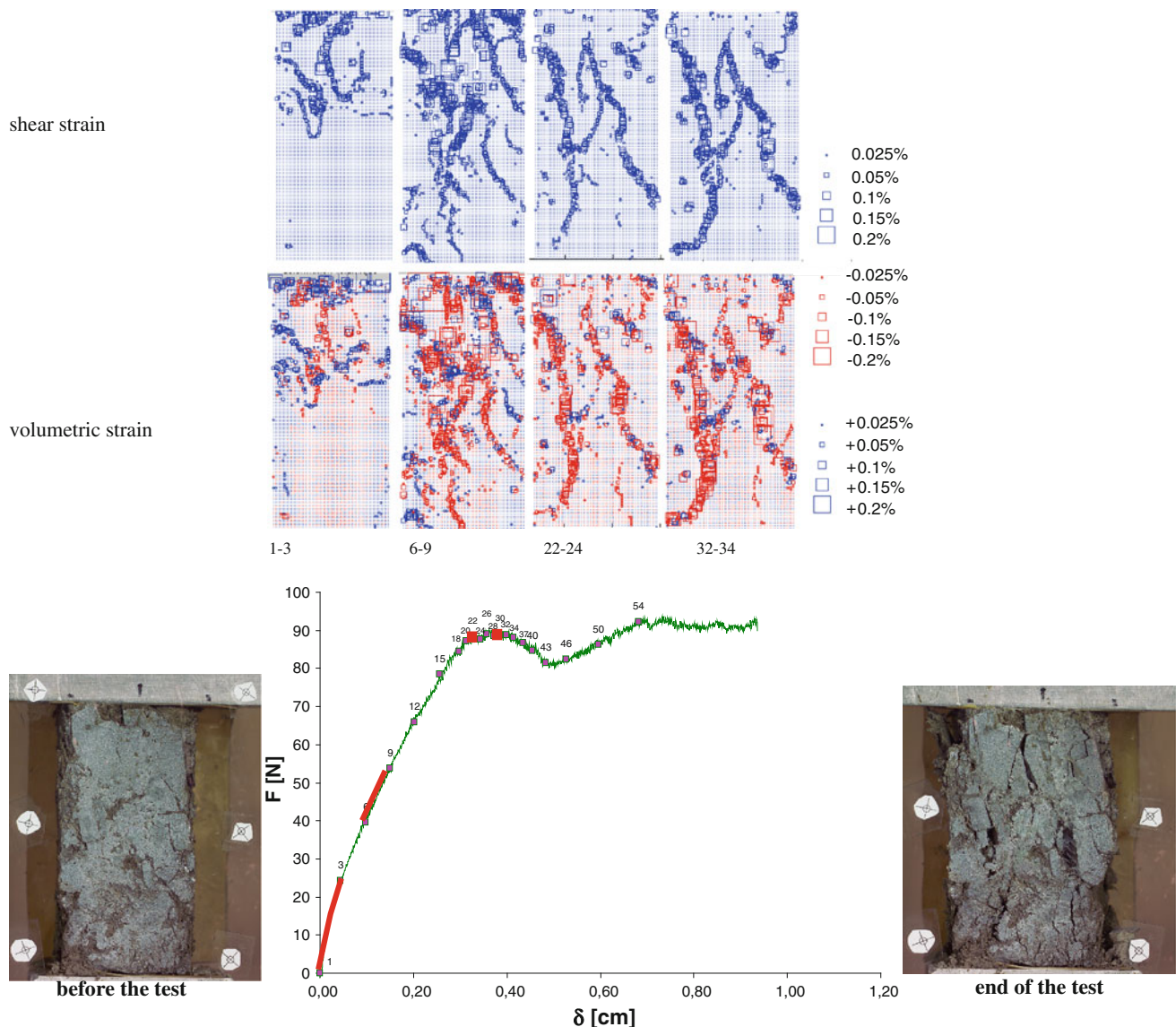Figure 13 shows the incremental strain fields obtained in test SV; this was the only (small) specimen containing

Fig. 13 Test SV. Load–displacement curve and DIC-derived shear and volumetric strain fields for selected load increments (in *red* along the *curve*) (color figure online)

vertical fissures. The pattern of deformation is very clear in this case: from the very beginning of the test, the process consisted in the activation of multiple preexisting subvertical fissures. Localization about these fissures started from the top, and some of them crossed the specimen almost entirely by increment 6–9, well before the peak. The final failure mode was essentially axial splitting along these activated fissures that first connected the top of the specimen to the bottom, although the mechanism was made somewhat more complex by a fissure network inclined to the vertical and connecting the active vertical fissures. As a result, fissure opening was accompanied by fissure sliding. The clay blocks in between the fissures remained essentially undeformed throughout the process.

6 Discussion of the results

According to the pattern of behavior emerging from the results presented in the previous sections, the orientation of the fissures in the specimen (with respect to the direction of loading) dictates the evolution of the deformation within the material and, in turn, affects the global specimen response. DIC provided a detailed picture of the processes occurring throughout the tests, from the early stages, when both closure and opening of preexisting fissures could be tracked, to the complete development of a sliding mechanism between near-rigid bodies. The DIC results here presented extend what found by Vitone et al. [40] when applying FRS to SCM scaly clay specimens with horizontal fissures (i.e., normal to the major

principal stress) to specimens whose fissures are close to horizontal (e.g., L-Sub). In particular, for sub-horizontal fissures (either F1-0° or F1-20°: specimens SH1, SH2, L-Sub), the deformation process exhibited by the specimens is not very different from that observed in unfissured clays (e.g., [35]). The results show that at the beginning of the test, deformation is diffuse although several localized areas of fissure closure can be observed. Before the stress peak, deformation either starts localizing or it becomes more intense in one of the numerous localized areas. Post-peak localized deformation develops further in the zone where it increased just before the peak, leading eventually to a relative sliding mechanism (see photograph in Fig. 8). The global peak strength is not affected by the size of the specimen, which confirms and extends previous findings on the same material (e.g., [38, 40]).

When the specimen contains fissures inclined about 30° to the horizontal (e.g., specimen S-Sub), the deformation process differs to such an extent that the preexisting fissuring orientation makes the specimen particularly prone to fail through a block sliding mechanism at early stages of shearing. For fissures inclined about 50° to the horizontal (e.g., specimens SM, LM), the deformation becomes localized almost immediately and consists essentially of the activation of the inclined fissures, which are all potential failure surfaces. Around the stress peak, one of the fissures eventually takes over to become *the* single sliding surface. In terms of the global response, specimens with fissures inclined from 30° to the horizontal exhibit lower stiffness, lower peak stress, and milder softening if compared to specimens with horizontal fissures.

When fissures are vertical, that is, parallel to the major principal stress, the deformation process consists of the activation of multiple preexisting sub-vertical fissures from the very beginning of test. The final failure mode is essentially axial splitting, with clay blocks in between the fissures remaining almost undeformed throughout the process. As expected, this case is characterized by the lowest strength and the least brittle response.

Similar results are reported by Vitone et al. [41] for plane strain compression tests carried out on specimens of fissured bentonite clay. In this case, the F-ID of the bentonite clay could be characterized by two levels of fissures (i.e., a first level, F3-I5, and a second one, more continuous and less intense, F2-I4). In particular, the second-level fissures inclined either about or higher than 30° to the horizontal were found to predispose the specimen to fail according to a block sliding mechanism that took control at early stages of shearing (see [41] for further details).

7 Conclusive remarks and future research

The effects of the combination of different factors, such as the specimen size and the orientation of fissuring, on the mechanical behavior of the intensely fissured scaly clay from Santa Croce di Magliano have been analyzed. This investigation has involved an experimental program using plane strain compression tests with the key aspect being that the standard global stress–strain response was augmented by full-field displacement and strain measurements through 2D DIC.

DIC revealed the internal processes generating the global responses and failure patterns observed with traditional element test monitoring. This is because DIC-derived incremental strain fields have allowed the deformation processes to be followed throughout each test, providing both spatial and temporal strain evolutions. A general first result that has to be mentioned is that DIC allowed to directly relate the local deformation patterns within the specimens to the observed increase in brittleness in the global behavior with decreasing inclination of the preexisting fissures.

The key conclusions from this work relating to fissure orientation and material failure are as follows: (1) for fissures oriented about normal to the major principal stress, the deformation process is not very different from that observed in unfissured clays, and the small size specimens are the REV of the material; (2) for fissures with an inclination either equal to or higher than 30° to the horizontal, the deformation process starts to be controlled by sliding along preexisting fissures, and such a behavior does not change with the specimen size (i.e., the small specimen is still the REV); (3) for fissures with an inclination of about 50° to the horizontal, size effect on the peak strength has been recorded but the small size specimen can still qualitatively represent the global behavior of the clay; (4) for vertical fissures (parallel to the maximum stress), multiple preexisting sub-vertical fissures are activated at the start of loading, the final failure mode is essentially axial splitting, and the strength is the minimum one.

In particular, the more the fissure orientation increases with respect to the horizontal, the more the strain localization process differs from that recorded for either horizontal fissuring or unfissured clays and consists in the activation of multiple preexisting fissures between near-rigid portions of the specimen from the very beginning of test. Correspondingly, in terms of global behavior, the more fissures are inclined from the horizontal, the more the clay strength reduces, and the clay behavior becomes less brittle.

Furthermore, access to incremental strain fields through DIC has provided information about the impact of anomalies in the test performance on the macroscopic behavior, such as that observed for tests implementing acoustic emissions. As such, local phenomena have enabled explanations of observed trends in global responses.

Further studies should apply DIC to tests carried out under confining stresses and with saturation and drainage
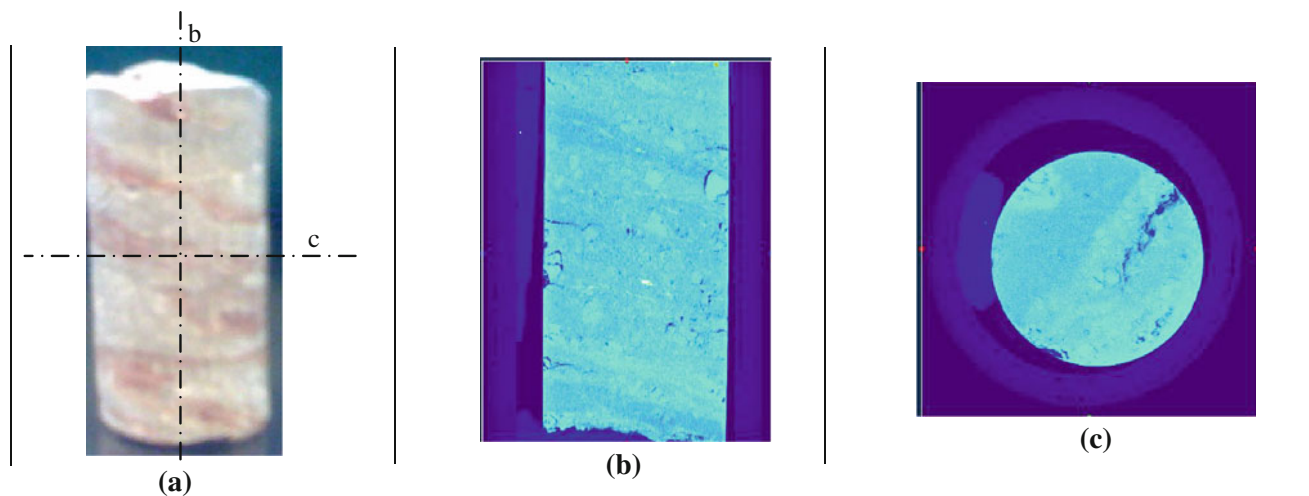
Fig. 14 Triaxial specimen of scaly clay **a** photograph and trace of the sections, **b** vertical, **c** horizontal tomographic slices

control, as both these factors are expected to influence strongly the (localized) deformation processes. These studies could be carried out under either plane strain or triaxial conditions. Furthermore, recent studies are showing the feasibility of the use of X-ray tomography to provide 3D images of a specimen throughout a triaxial test. As an example, a first result of the application of X-ray tomography to a triaxial specimen of scaly clay (20 mm diameter) is reported in Fig. 14 (a voxel size of 14 μm was achieved). Just scanning the undisturbed specimen, from the two cross-sectional tomographic slices (Fig. 14b, c), it appears that open fissures are clearly visible, even if located inside the specimen. It follows that the use of 3D DIC during triaxial loading could give 3D incremental strain measurements (e.g., [19]), both to detect the onset of strain localization and to characterize its development in 3D (including the interaction with preexisting fissures).

References

1. AGI (1979) Some Italian experiences on the mechanical characterisation of structurally complex formations. In: International Society of Rock Mechanics (ed) Proceedings of the 4th international congress of the international society of rock mechanics, Montreux, vol 1, pp 827–846
2. AGI (1985) Geotechnical properties and slope stability in structurally complex clay soils. Geotech Eng Italy 2:189–225
3. Airò Farulla C, Nocilla N (1984) Assetto strutturale e resistenza a taglio dei campioni di argille a scaglie. Rivista Italiana di Geotecnica 3:148–158
4. Bilotta E (1987) Contributo allo studio della resistenza al taglio di argille a scaglie con prove di laboratorio. Rivista Italiana di Geotecnica 133–143
5. Bishop AW (1967) Progressive failure, with special reference to the mechanism causing it. Proc Geotech Conf Oslo 2:3–10
6. BS 8004 (1986) Code of practice for foundations. British Standard Institutions, London
7. Chen J, Zhang X, Zhan N, Hu X (2010) Deformation measurement across crack using two-step extended digital image correlation. Opt Lasers Eng 46:746–757
8. Cotecchia F, Vitone C, Cafaro F, Santaloia F (2006) The mechanical behaviour of intensely fissured high plasticity clays from Daunia. Invited paper. In: Second international workshop on characterisation and engineering properties on natural soils, Singapore, pp 1975–2003
9. Cotecchia F, Vitone C (2011) On the model requirements to predict the behaviour of fissured clays. In: Proceedings of the XV European conference on soil mechanics and geotechnical engineering, Athens, Greece, pp 525–530
10. Cotecchia V, Valentini A (1973) Comportamento allo scavo in galleria di rocce argillose tipiche dell'Appennino meridionale. Geologia Applicata e Idrogeologia 3:347–385
11. Croce A (1971) Opening address of the international symposium on "the geotechnics of structurally complex formations", Capri, vol II, pp 148–151
12. Dazzaro L, Rapisardi L (1996) Schema geologico del margine appenninico tra il F. Fortore e il F. Ofanto. Memorie Società Geologica Italiana 51:143–147
13. Desrues J, Viggiani G (2004) Strain localization in sand: an overview of the experimental results obtained in Grenoble using stereophotogrammetry. Int J Numer Anal Methods Geomech 28:279–321
14. Doglioni C (1991) A proposal for the kinematic modelling of W-dipping subductions—possible applications to the Tyrrhenian-Apennines system. Terra Nova 3:423–434
15. Fenelli GB, Picarelli L, Silvestri F (1992) Deformation process of a hill shaken by Irpinia earthquake in 1980. In: Proceedings of the French-Italian conference on slope stability in seismic areas, Borfighera, pp 47–62
16. Fookes PG, Denness B (1969) Observational studies on fissure patterns in cretaceous sediments of South-East England. Géotechnique 19(4):453–477

17. Grégoire D (2008) Initiation, propagation, arrêt et redémarrage de fissures sous Impact. Ph.D thesis, Institut National de Sciences Appliqués de Lyon, Lyon, France
18. Guler M, Edil TB, Bosscher PJ (1999) Measurement of particle movement in granular soils using image analysis. J Comput Civil Eng ASCE 13(2):116–122
19. Hall SA, Bornert M, Desrues J, Pannier Y, Lenoir N, Viggiani G, Besuelle P (2010) Discrete and continuum analysis of localised deformation in sand using X-ray μCT and volumetric digital image correlation. Géotechnique 60(5):315–322
20. ISRM (1993) Metodologie per la descrizione quantitativa delle discontinuità nelle masse rocciose. Rivista Italiana di Geotecnica 2:151–197
21. Malinverno A, Ryan WBF (1986) Extension in the Tyrrhenian Sea and shortening in the Apennines as result of arc migration driven by sinking of the lithosphere. Tectonics 5:227–245
22. Mastropierro L (2009) DIC techniques to characterize displacement or deformation fields for natural specimens of fissured clays during biaxial compression. Master thesis in Mécanique, Energétique et Ingénieries Spécialité Modélisation et Expérimentation en Mécanique des Solides (International path: Geomechanics, Civil Engineering and Risks) Université Joseph Fourier—Grenoble INP, France
23. Melidoro A, Melidoro G, Panaro V (2002) Deformazioni gravitative dei versanti nei terreni flisciodi con argille a bentoniti di Santa Croce di Magliano (Molise). Quarr Constr 2:11–17
24. Morgenstern NR, Eigenbrod KD (1974) Classification of argillaceous soils and rocks. J Geotech Eng Div ASCE 100(10):1137–1156
25. Nguyen TL, Hall SA, Vacher P, Viggiani G (2011) Fracture mechanisms in soft rock: identification and quantification of evolving displacement discontinuities by extended digital image correlation. Tectonophysics 503:117–128
26. Picarelli L, Olivares L, Di Maio C, Silvestri F, Di Nocera S, Urciuoli G (2003) Structure properties and mechanical behaviour of the highly plastic intensely fissured Bisaccia clay shale. In: Tan TS, Phoon KK, Hight DW, Leroueil S (eds) Characterisation and engineering properties of natural soils: proceedings of the international workshop. A.A. Balkema, Rotterdam, The Netherlands, pp 947–982
27. Poissant J, Barthelat F (2010) A novel "subset splitting" procedure for digital photograph correlation on discontinuous displacement fields. Exp Mech 50:353–364
28. Rechenmacher AL, Abedi S, Chupin O (2011) Characterization of mesoscale instabilities in localized granular shear using digital image correlation. Acta Geotech 6:205–217
29. Réthoré J, Gravouil A, Morestin F, Combescure A (2005) Estimation of mixed-mode stress intensity factors using digital image correlation and an interaction integral. J Fract 132:65–79
30. Réthoré J, Hild F, Roux S (2007) Shear-band capturing using a multiscale extended digital image correlation technique. Comput Methods Appl Mech Eng 196:5016–5030
31. Réthoré J, Hild F, Roux S (2008) Extended digital image correlation with crack shape optimization. Int J Numer Methods Eng 72:248–272
32. Roux S, Hild F (2006) Stress intensity factor measurements from digital image correlation: post-processing and integrated approaches. J Fract 140:141–157
33. Terzaghi K (1936) Stability of slopes in natural clays. In: Proceedings of the 1st conference on soil mechanics, Harvard, vol 1, pp 161–185
34. Vacher P, Dumoulin S, Morestin F, Mguil-Touchai S (1999) Bidimensional strain measurement using digital images. Proc Inst Mech Eng Part C 213:811–817
35. Viggiani G, Desrues J (2004) Experimental observation of shear banding in stiff clay. In: Brinkgreve RBJ et al (eds) Geotechnical innovations (studies in honour of Prof. Pieter A. Vermeer on occasion of his 60th birthday). Verlag Glückauf, Essen, pp 649–658
36. Viggiani G, Hall SA (2008) Full-field measurements, a new tool for laboratory experimental geomechanics. In: Burns SE, Mayne PW, Santamarina JC (eds) Fourth symposium on deformation characteristics of geomaterials, Atlanta, USA, vol 1. IOS Press, Amsterdam, pp 3–26
37. Vitone C (2005) Comportamento meccanico di argille da intensamente a mediamente fessurate. PhD thesis, Technical University of Bari, Italy
38. Vitone C, Cotecchia F (2011) The influence of intense fissuring on the mechanical behaviour of clays. Géotechnique 61(12):1003–1018
39. Vitone C, Cotecchia F, Santaloia F, Cafaro F (2005) Preliminary results of a comparative study of the compression behaviour of clays of different fissuring. In: Proceedings of the international conference on problematic soils—GEOPROB2005, Cyprus, pp 1173–1181
40. Vitone C, Cotecchia F, Desrues J, Viggiani G (2009) An approach to the interpretation of the mechanical behaviour of intensely fissured clays. Soils Found 49:355–368
41. Vitone C, Cotecchia F, Viggiani G, Hall SA (2012) Strain fields and mechanical response of a high to medium fissured bentonite clay. Int J Numer Anal Methods Geomech. Published online: Wiley Online Library (wileyonlinelibrary.com). doi:10.1002/nag.2095
42. Walker BF, Blong RJ, McGregor JP (1987) Landslide classification, geomorphology and site investigation. Soil slope instability and stabilisation. Balkema, Rotterdam, pp 1–52
43. White DJ, Take WA, Bolton MD (2003) Soil deformation measurement using particle image velocimetry (PIV) and photogrammetry. Géotechnique 53(7):619–631
44. Yoneyama S, Ogawa T, Kobayashi Y (2007) Evaluation mixed-mode stress intensity factors from full-field displacement fields obtained by optical methods. Eng Fract Mech 74:1399–1412